Received: 26 August 2021 | Revised: 20 October 2021 | Accepted: 16 November 2021

DOI: 10.1111/jace.18271

Journal of the American Ceramic Society

RESEARCH ARTICLE

Reactions of metal chlorides with hexamethyldisilazane: Novel precursors to aluminum nitride and beyond

Xinyu Zhang[1] | **Mengjie Yu**[2] | **Sylvio Indris**[3] | **Richard M. Laine**[1,2]

[1] Department of Materials Science and Engineering, University of Michigan, Ann Arbor, Michigan, USA

[2] Department of Macromolecular Science and Engineering, University of Michigan, Ann Arbor, Michigan, USA

[3] Institute for Applied Materials, Karlsruhe Institute of Technology, Eggenstein-Leopoldshafen, Germany

Correspondence
Richard M. Laine, Macromolecular Science and Engineering, University of Michigan, Ann Arbor, MI 48109-2136, USA.
Email: talsdad@umich.edu

Funding information
NSF DMR, Grant/Award Number: 1926199

Abstract

Metal nitrides are intensely investigated because they can offer high melting points, excellent corrosion resistance, high hardness, electronic and magnetic properties superior to the corresponding metals/metal oxides. Thus, they are used in diverse applications including refractory materials, semiconductors, electronic devices, and energy storage/conversion systems. Here, we present a simple, novel, scalable and general route to metal nitride precursors by reactions of metal chlorides with hexamethyldisilazane [HMDS, $(Me_3Si)_2NH$] in tetrahydrofuran or acetonitrile at low temperatures (ambient to 60°C/N_2). Such reactions have received scant attention in the literature.

The work reported here focuses primarily on the Al-HMDS precursor produced from the reaction of $AlCl_3$ with HMDS (mole ratio = 1:3) characterized by matrix-assisted laser desorption/ionization-time of flight, Fourier-transform infrared spectroscopy, thermogravimetric analysis-differential thermal analysis, and multinuclear nuclear magnetic resonance spectroscopy (NMRs) for chemical and structural analyses. The Al-HMDS precursor heated to 1600°C/4 h/N_2 produces aluminum nitride, characterized by X-ray powder diffraction, X-ray photoelectron spectroscopy, scanning electron microscopy/energy-dispersive X-ray spectroscopy, and magic-angle spinning NMR. On heating to 800–1200°C/4 h/N_2, the precursor transforms to an amorphous, oxygen-sensitive powder with very high surface areas (>200 m^2/g) indicating nanosized particles, which can be used as additives to polymer matrices to modify their thermal stabilities. Al_2O_3 is also presented in the final product after heating, due to its high susceptibility to oxidation.

This approach was extended via proof-of-concept studies to other metal chloride systems, including Zn-HMDS, Cu-HMDS, Fe-HMDS, and Bi-HMDS. The formed precursors are volatile, offering the potential utility as gas-phase deposition precursors for their corresponding metal nitrides.

KEYWORDS
aluminum nitride, hexamethyldisilazane, metal chlorides, metal nitrides, precursors

1 | INTRODUCTION

Metal nitrides, in comparison to oxides, are richer in their bonding schemes as more electrons are present in the bonds than are localized on the anion lattice, reflecting in their electronic and optical properties.[1,2] Metal nitrides are well known to offer very high melting points, excellent corrosion resistance, high hardness, and mechanical strength, but are also brittle, typical ceramic materials.[1,3] In addition, many metal nitrides are conductors/semiconductors with electronic properties exceeding their parental metals, making them alternatives to pure elemental metals and metal oxides.[1,4,5] As a result, metal nitrides are used in a variety of applications, including long-lasting hard coatings,[3,6] refractory materials,[3,7] semiconductors,[8–10] diffusion barriers in electronic devices,[3,8,11] and energy storage, and conversion systems.[5,12–14]

Among the metal nitrides, aluminum nitride (AlN) shows high thermal conductivity (~180 W/mK), negligible electrical conductivity (10^{-13}–10^{-11} S/cm), relatively high electrical breakdown voltage (12–18 kV/mm), piezoelectric properties with wide bandgap (~6 eV), good mechanical strength (e.g., flexural strength ~350 MPa) and high hardness (1000 kg/mm^2). As a ceramic, it suffers solely from low fracture toughness of 3–3.5 MPa m$^{1/2}$.[15–17] As a result, AlN can be used in power electronic substrates,[18,19] semiconductors,[10,20] active materials for microelectromechanical systems[15,21,22] and deep-ultraviolet optoelectronic applications.[23,24]

Common AlN powder synthesis methods include direct nitridation and carbothermal reduction; Equations (1) and (2), respectively.[25,26] During direct nitridation, aggregates form easily as molten Al powder is used, mandating intermediate pulverizing (e.g., ball milling) to minimize average particle sizes (APSs), often with concomitant contamination.

The milling step often leads to surface oxidation, resulting in O contents of 2–5 wt.%. Furthermore, unreacted metallic Al is typically included, and acid washing is needed.[25,26] For carbothermal reduction methods, high temperatures are required (typically 1500–1700°C) and toxic CO gas is produced. Excess carbon is generally required to achieve full conversion, and a carbon burnout step is required (typically 600–900°C in dry air), which also introduces oxygen impurities.[25,26]

$$2\mathrm{Al}\,(l) + \mathrm{N_2}\,(g) \xrightarrow{\geq 1200^\circ\mathrm{C}} 2\mathrm{AlN}\,(s) \qquad (1)$$

$$\mathrm{Al_2O_3} + 3\mathrm{C} + \mathrm{N_2} \xrightarrow{\sim 1600^\circ\mathrm{C}} 2\mathrm{AlN} + 3\mathrm{CO} \qquad (2)$$

To produce fully dense monolithic products, the as-synthesized powders are then subjected to green processing prior to sintering, typically tape casting using organic solvents with plasticizers and binders.[25] Such a process must be carefully controlled as AlN undergoes low-temperature hydrolysis. The sintering of AlN generally requires high temperatures of 1750–1900°C with sintering aids such as Y_2O_3 or CaO.[25,26]

More recent AlN synthesis methods involve gas phase deposition for electronic device applications, such as reactive magnetron sputtering,[15,27] chemical vapor deposition,[28,29] molecular beam epitaxy,[30–32] pulsed laser deposition,[33,34] atomic layer epitaxial,[35,36] and so forth. In general, gas-phase deposition offers impurity-free products with perfectly defined structures. However, commodity scale production is challenging given the required specialized and expensive apparatus and low production rates (generally < 100 nm/min).[37–39]

Here, we report a simple reaction of $AlCl_3$ with hexamethyldisilazane [HMDS, $(Me_3Si)_2NH$] in tetrahydrofuran (THF) or acetonitrile (ACN) at 60°C/N_2 to produce an AlN precursor, $Al(NHSiMe_3)_3$ (denoted as Al-HMDS for convenience), as suggested by reaction (3). The byproduct Me_3SiCl (boiling point = 57°C) can be removed easily along with THF/ACN and excess HMDS by drying at 80°C/1 h/vacuum (vac). The dried Al-HMDS precursor can be further heated to 1600°C/4 h/N_2 in a tube furnace to produce AlN, characterized by various analytical methods including X-ray powder diffraction (XRD), X-ray photoelectron spectroscopy (XPS), scanning electron microscopy/energy-dispersive X-ray spectroscopy (SEM/EDX), and magic-angle spinning nuclear magnetic resonance spectroscopy (MAS NMR). However, as discussed below, the heated products are highly susceptible to oxidation due to their quite high surface areas (>200 m^2/g), and therefore it is hard to eliminate oxidation products typically in the form of Al_2O_3. Process optimization needs further attention; however, this approach should offer the potential for making coatings and, as we show in preliminary examples, seems to be a general, low cost, and low-temperature approach to making a variety of metal nitrides.

The high surface areas are indicative of nanoscale particles. We show that the heated Al-HMDS powders can be used as additives to polymer matrices to modify their thermal stabilities, offering another potential application.

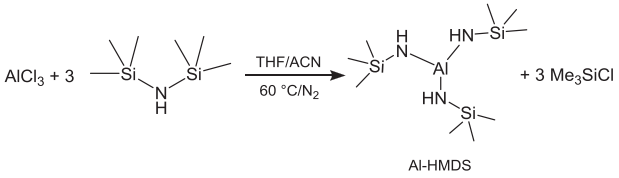

(3)

s-block complexes

$$2Li + BuX \rightarrow {}^{n}BuLi + LiX$$
(Bu = C_4H_9, X = Cl, Br)

$${}^{n}BuLi + NH(SiMe_3)_2 \rightarrow Li(hmds) + C_4H_{10}$$

Or

$$M + NH(SiMe_3)_2 \rightarrow M(hmds) + \tfrac{1}{2}\, H_2$$

d-block complexes

$$MCl_3 + 3Li(hmds) \rightarrow M(hmds)_3 + 3LiCl$$
(M = Sc, Ti, V, Cr, Fe, etc.)

p-block complexes

$$LiAlH_4 + 4NH(SiMe_3)_2 \rightarrow Li(hmds) + Al(hmds)_3 + 4H_2$$

SCHEME 1 Examples of different $M(HDMS)_x$ syntheses

In related work, Riedel et al.[40] describe the reaction of a 1:1 $AlCl_3$:HMDS molar ratio at 140°C under argon (Ar) to form $Cl_2AlNHSiMe_3$ (as a dimer), shown as reaction (4). To obtain AlN, the product was first heated at 1000°C/1 h/Ar and then annealed in an ammonia flow at 1000–1100°C/5–6 h. However, to eliminate the Cl content, the product required heating to 1200°C/Ar/7 h. Oxygen contamination was also a serious issue due to high moisture sensitivity.[40] To our knowledge, this is the only other effort targeting production of AlN (or other nitrides) using HMDS or Me_3SiCl as a leaving group reported to date, despite its obvious simplicity.

$$AlCl_3 + HN(SiMe_3)_2 \xrightarrow{140°C/Ar} \frac{1}{2}[Cl_2AlNHSiMe_3]_2 + Me_3SiCl \quad (4)$$

In comparison, our proposed synthesis runs at a lower temperature (up to 60°C) in a solvent with simple heating to give an AlN precursor (and other metal nitride precursors, see section 3.3) that can generate nanosized particles, likely can be used for coating purposes directly from solution and has the advantage of avoiding some of the important issues noted in the introduction.

In contrast to the Riedel et al.[40] work, we find that a 3:1 mole ratio of HMDS to $AlCl_3$ helps minimize Cl retention. We were also able to extend our study to different metal-HMDS (M-HMDS) systems, including Zn-HMDS, Cu-HMDS, Fe-HMDS, and Bi-HMDS, as potential precursors to metal nitrides.

It is important to note that the present M-HMDS systems differ from traditional metal hexamethyldisilazides, $M[N(SiMe_3)_2]_x$, typically discussed as $M(hmds)_x$. Some examples of $M(HDMS)_x$ syntheses are presented in Scheme 1. Alkali M(HDMS) (M = Li, Na) is typically synthesized from ^{n}BuM with HMDS, where ^{n}BuM is obtained by reacting alkali metal with chloro/bromobutane.[41–43] Alkali M(HMDS) can then be reacted with metal halides to produce different $M(HMDS)_x$, including transition metal complexes.[44,45] One-step direct reactions of metals with HMDS are also used to synthesize some s-block $M(HMDS)_x$ (typically for M = Rb, Cs).[46,47] However, the use of highly reactive Rb or Cs metal and the generated H_2 gas requires additional safety measures. For p-block complexes such as $Al(HDMS)_3$, $LiAlH_4$ is used, which reacts exothermically with water and releases H_2.

In comparison, our proposed reactions of MCl_x with HMDS involve only single-step syntheses and avoid the use of alkali metals and other hazardous chemicals. Such reactions have received little attention in the literature, hence the further motivation for the work presented here.

2 | EXPERIMENTAL PROCEDURE

2.1 | Materials

All chemicals and solvents were obtained from commercial suppliers. Anhydrous $AlCl_3$ and $FeCl_3$ were purchased from Acros Organics. HMDS and anhydrous $BiCl_3$ were obtained from Alfa Aesar. Anhydrous $ZnCl_2$ was purchased from Honeywell Fluka. THF, ACN, and $CuCl_2$ were supplied by Sigma-Aldrich.

2.2 | Syntheses of M-HMDS complexes

In general, M-HMDS complexes are synthesized by reactions between metal chlorides with HMDS. Since metal chlorides are typically hygroscopic, they were first dried by reaction with $SOCl_2$ or by simply heating at ~120°C/vacuum/24–48 h to remove adsorbed moisture. This step was followed by a reaction with HMDS in THF or ACN. An exemplary synthesis of Al-HMDS is given below.

2.2.1 | Synthesis of Al-HMDS

In a 200 ml Schlenk flask equipped with a magnetic stirrer, $AlCl_3$ (4 g, 0.03 mol) was first added to $SOCl_2$ (5 ml, 0.07 mol) for drying. The mixture was kept under N_2 flow overnight connected to a NaOH aqueous solution to trap HCl and SO_2. It was then heated to 70°C/24 h/N_2 to remove $SOCl_2$. Thereafter, to the dried $AlCl_3$, 80 ml distilled THF and HMDS (22 ml, 17.0 g, 0.11 mol) were added via graduated pipettes under N_2. The mole ratio of HMDS to $AlCl_3$ is

TABLE 1 Syntheses of metal-hexamethyldisilazane (M-HMDS) precursors

-HMDS	MCl_x/HMDS molar ratio	Solvent used	Reaction appearance	Dried product appearance
Al-	3.5	THF or ACN	Dark red/brown solution	Yellow/orange solid
Zn-	2.5	THF or ACN	Transparent solution	Yellow/orange viscous liquid
Cu-	2.5	THF	Brown solution + green solid	Solute: brown solidInsoluble part: green solid
Fe-	3.5	ACN	Brown solution	Dark brown solid viscous liquid
Bi-	3.5	ACN	Transparent solution + white/light-yellow solid	Soluble and insoluble parts: light-yellow solid

Abbreviations: ACN, acetonitrile; THF, tetrahydrofuran.

3.5. The reaction was kept running at 60°C/N_2/3 days with a reflux condenser connected. Figure S1 shows a representative reaction mixture of the Al-HMDS precursor synthesis.

To obtain the yield, a small sample (5 ml) was transferred to a 25 ml Schlenk flask and vacuum dried at 80°C/1 h to remove solvent and unreacted HMDS, which gave a yellow solid (0.3 g). The total yield was calculated to be 6.1 g, which is ~70 % of the theoretical yield (8.7 g).

2.2.2 | Other M-HMDS precursor syntheses

Representative reaction mixtures of other M-HMDS precursor syntheses are shown in Figures S2A-D. Zn-HMDS and Fe-HMDS reactions generate clear solutions, while Cu-HMDS and Bi-HMDS reaction mixtures remain as suspensions. Therefore, centrifugation was run on Cu-HMDS and Bi-HMDS reactions to separate the soluble and insoluble parts, and they were vacuum dried separately at 80°C/1 h for further characterization.

Table 1 summarizes MCl_x/HMDS molar ratios, typical solvents used, and appearances for different M-HMDS precursor syntheses. Detailed analytical methods are provided in the Supporting Information (SI).

The following sections focus primarily on reactions of $AlCl_3$ with HMDS targeting identification and characterization of intermediates and products by matrix-assisted laser desorption/ionization-time of flight (MALDI-ToF), Fourier-transform infrared spectroscopy (FTIR), thermogravimetric analysis (TGA), and differential thermal analysis (DTA), and multinuclear NMRs. To produce AlN, the precursors were heated to different temperatures (800–1600°C under N_2), followed by characterization using XRD, XPS, SEM/EDX, and MAS NMR.

We then used high surface areas (>200 m^2/g) Al-HMDS (800°C/4 h/N_2) powders with two different polymer matrices, exploring their potential utility to modify polymer thermal properties.

Finally, we present proof-of-concept efforts with other metal chlorides, including Zn-HMDS, Cu-HMDS, Fe-HMDS, and Bi-HMDS, characterized by FTIR, MALDI-ToF, multinuclear NMRs, and TGA-DTA.

3 | RESULTS AND DISCUSSION

3.1 | Characterization of Al-HMDS

The molecular weights and chemical structures of the Al-HMDS precursor were analyzed by both negative- and positive-ion MALDIs. The ion source in the negative-ion mode comes directly from the precursor when it loses Al^{3+}. The ion source for the positive-ion mode is Ag^+ from $AgNO_3$. Possible structures were predicted using a Python program, MALDI-Calculation (see SI). Similar MALDI analyses were done previously on Li_xPON-like and Li_xSiON precursors for lithium-ion battery applications.[37,38,48]

Figure 1A,B shows negative- and positive-ion MALDIs of the Al-HMDS precursor, respectively. Both exhibit oligomeric peaks in the range of 300–500 m/z. Possible structural components and composition calculations are given in Scheme S1 and Table S1, respectively. Predicted example structures based on MALDI analyses are shown in Figure 1C.

Overall, both ion mode MALDI spectra show peaks that can be ascribed to 2–4 units containing Al-N bonds, suggesting oligomers and/or cyclomers with Al-N backbones, Figure 1C. Some peaks also indicate -Cl inclusion and complexes with THF, consistent with NMR and EDX studies below.

Chemical environments were characterized by ^1H and ^{29}Si NMRs on both the reaction mixtures (50 μl THF solution in 1 ml $CDCl_3$) and dried Al-HMDS precursor (0.1 g/ml in $CDCl_3$).

As shown in Figure 2A, the dried Al-HMDS shows groups of small peaks at 3.7, 3.4 ppm and 1.8, 1.6 ppm,

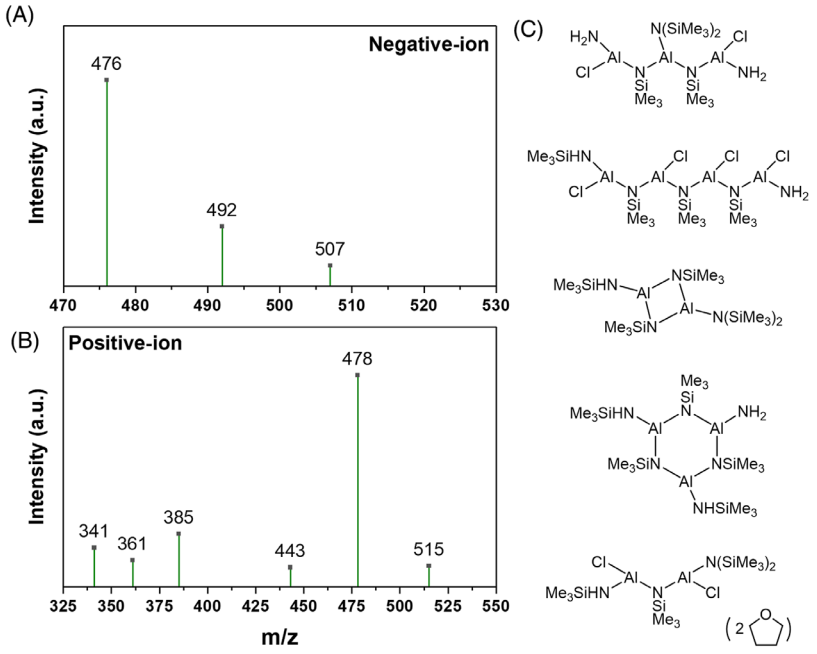

FIGURE 1 Negative- (A) and positive- (B) ion mode example structures based on matrix-assisted laser desorption/ionization (MALDIs) of the Al-HMDS precursor and predicted MALDI calculations (C)

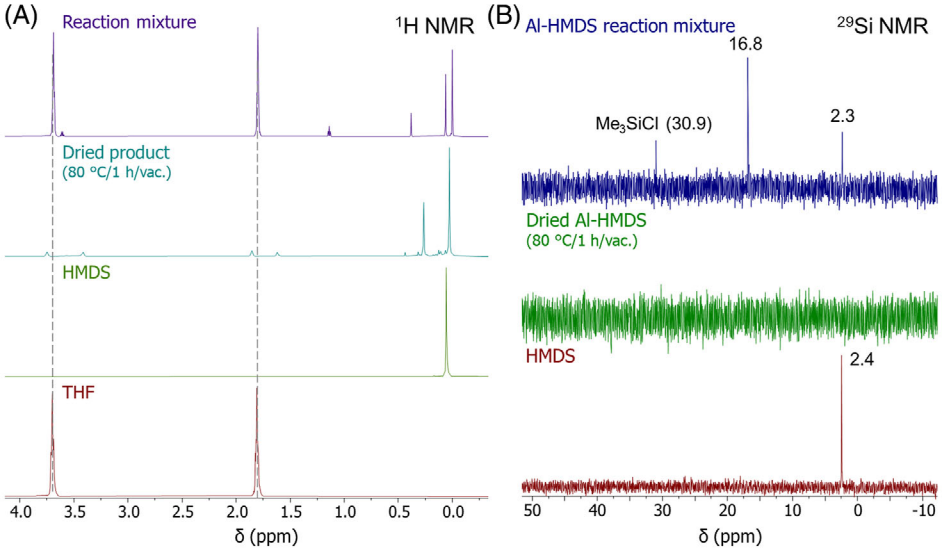

FIGURE 2 ^{1}H (A) and ^{29}Si (B) nuclear magnetic resonance (NMR) spectra of the Al-HMDS precursor solution before and after drying (80°C/1 h/vac), compared to hexamethyldisilazane (HMDS) and tetrahydrofuran (THF)

suggesting the presence of -C**H**$_2$O (3.7 ppm) and -C**H**$_2$ (1.8 ppm) from THF, perhaps derived from reaction or complexation with THF, corresponding to MALDI analyses above. Similarly, the reaction mixture also shows small peaks at 3.6 and 1.1 ppm in addition to THF peaks, likely from Al^{3+}-THF complexes that shifted due to solvent effects.

In addition, the dried product shows two major -C**H**$_3$ peaks at 0.03 and 0.27 ppm. The peak at 0.03 ppm may be from excess HMDS (0.06 ppm), or -NHSi**Me**$_3$ group similar to HMDS. The peak at 0.27 ppm can be ascribed to Al-NSi**Me**$_3$ units from the Al-HMDS product. The downfield shift is likely a result of the interaction of -N(H)Si**Me**$_3$ with Al^{3+}.

Similarly, the reaction mixture shows methyl peaks at 0, 0.07, and 0.4 ppm. The peak at 0.4 ppm can be ascribed to **Me**$_3$SiCl. The two peaks at 0 and 0.07 ppm are suggested to be -NHSi**Me**$_3$ and Al-NSi**Me**$_3$, respectively. Compared to the dried product, the two peaks shift upfield due to solvent effects.

Figure 2B compares ^{29}Si NMR spectra of Al-HMDS and HMDS. No peaks were observed for the dried product, likely due to low solubility and/or fluxional behavior.[48] For the reaction mixture, three ^{29}Si peaks appear at 2.3, 16.8,

TABLE 2 Evolution of Al-HMDS pellets heated to 800° and 1600°C/4 h/N_2

	800°C/4 h/N_2	1600°C/4 h/N_2
Mass loss (wt.%)	67 ± 0.9	74 ± 2.1
Vol.% shrinkage	69 ± 2.4	80 ± 2.2
Green density (g/cm^3)	1.3 ± 0.01	1.3 ± 0.03
Final density (g/cm^3)	1.4 ± 0.07	1.6 ± 0.08
Density increase (%)	7 ± 5.3	27 ± 6.0

TABLE 3 Average specific surface areas (SSAs), pore diameters, and average particle sizes (APSs) of Al-HMDS powders heated to different temperatures

	SSA (m^2/g)	Average pore diameter (nm)	APS (nm)
800°C/4 h/N_2	252	4.4	17
1200°C/4 h/N_2	228	5.2	19
1600°C/4 h/N_2	28	16	133

and 30.9 ppm. The peaks at 2.3 and 30.9 ppm are assumed to be -NH**Si**Me_3 (similar to HMDS) and Me_3**Si**Cl,[49] respectively, consistent with ^{1}H NMR data above. The peak at 16.8 ppm is likely from Al-N**Si**Me_3. Similar to ^{1}H NMR, the Al-N**Si**Me_3 peak from the product shifts downfield compared to -NH**Si**Me_3 due to interaction with Al^{3+}.

Overall, NMR studies show good agreement with MALDI analyses on the as-synthesized Al-HMDS precursor. To further characterize the properties of Al-HMDS after heating, the dried Al-HMDS (80°C/1 h/vac) was then pelletized hydraulically at 5 ksi/1 min at room temperature (RT) and heated to 800–1600°C/4 h/N_2 in a graphite boat in a tube furnace. Figure S3 compares Al-HMDS pellets after heating to different temperatures.

As listed in Table 2, the pellets heated to 800°C/4 h/N_2 show lower mass loss, volume shrinkage, and density increases compared to pellets heated to 1600°C/4 h/N_2. The mass loss at 800°C corresponds to a ceramic yield (CY, 33 %) from TGA (Figure S4).

Density increases after heating to both 800° and 1600°C/4 h/N_2, suggesting densification occurs with increasing temperature, as expected and discussed below.

Al-HMDS powders were also heated to 800–1600°C/4 h/N_2 for specific surface areas (SSAs) analysis by Brunauer, Emmett and Teller (BET) theory. Table 3 compares SSAs, average pore diameters, and APSs of Al-HMDS powders heated to different temperatures. Al-HMDS heated to 800° or 1200°C show similar SSAs >200 m^2/g. On heating to 1600°C, the resulting powders exhibit a much-reduced SSA of 28 m^2/g coincident with grain growth. The high SSAs at 800° and 1200°C indicate small pore sizes (4–5 nm) and APSs of ~20 nm.

TABLE 4 Phase contents (wt.%) from X-ray powder diffraction (XRD) quantitative analyses of Al-HMDS pellets heated to 1600°C/2, 4 h/N_2

Phase	Content (wt.%)	
Condition	1600°C/2 h/N_2	1600°C/4 h/N_2
Al_2O_3	89	55
AlN	11	45

Abbreviation: AlN, aluminum nitride.

As discussed above, Al-HMDS pellets heated to 1600°C/4 h/N_2 exhibit ~27 % density increase corresponding to the reduced SSAs. XRD data for lower temperatures show primarily amorphous materials and only at 1600°C are clear crystalline peaks for AlN observed, see below.

Figure 3A compares FTIRs of Al-HMDS heated to 80–600°C. Similar spectra are seen after heating to ≤200°C: broad νN-H/O-H peak centered at 3100/cm, νC-H at the right of 3000/cm, a small N-H/O-H overtone at 1640/cm, δN-H/C-H at ~1400/cm, and νSi-CH_3 at ~1250/cm. On heating to 300°C, peak intensities for νC-H, δN-H/C-H, and νSi-CH_3 start to decrease, suggesting decomposition of organic components, corresponding to the major mass loss at ~250°C from TGA (Figure S4).

The νN-H/O-H peak intensity decreases as temperature increases. When heated to 600°C, there is mainly a broad peak at ~600-800/cm, likely C, SiC, AlN, and/or νAl-O.[50–52]

When heated to 800–1600°C/N_2, similar peaks at ~600–800/cm are observed, Figure 3B. Only after heating to 1600°C/4 h/N_2 do peaks separate at ~500/cm with sharper features, suggesting increased crystallinity compared to Al-HMDS heated to lower temperatures, as confirmed by XRD studies below.

As shown in Figure 4A, Al-HMDS pellets heated to 800–1200°C/4 h/N_2 show amorphous diffraction patterns, with small α-Al_2O_3 peaks observed for pellets heated to 1200°C. When heated to 1600°C/2 h/N_2, a mixture of α-Al_2O_3 and wurtzite AlN phases are exhibited, and the AlN phase intensity increases with prolonged heating (1600°C/4 h/N_2). As given in Table 4, the AlN phase content increased from 11 to 45 wt.% when the heating time increased from 2 to 4 h. The presence of Al_2O_3 is likely due to moisture uptake as Al-HMDS shows high SSAs, discussed above, making it highly susceptible to oxidation. Similar results were reported by Riedel et al.[40] It's also possible that AlN is not fully crystallized, resulting in lower apparent content.

Figure 4B shows ^{27}Al MAS NMR spectra of Al-HMDS powders heated to different temperatures. After drying at

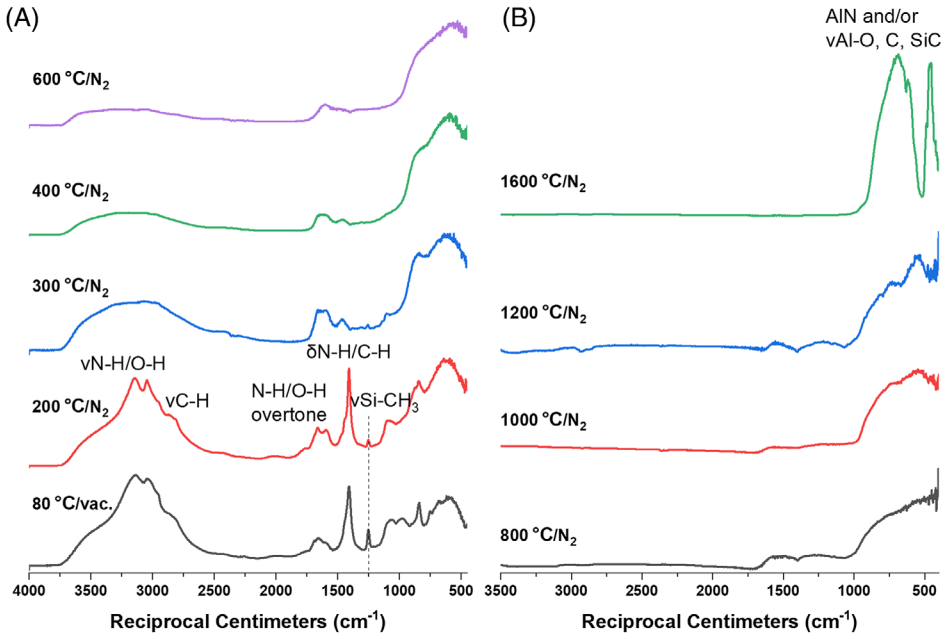

FIGURE 3 Fourier-transform infrared spectroscopy (FTIRs) of Al-HMDS heated to (A) 80–600°C and (B) 800–1600°C

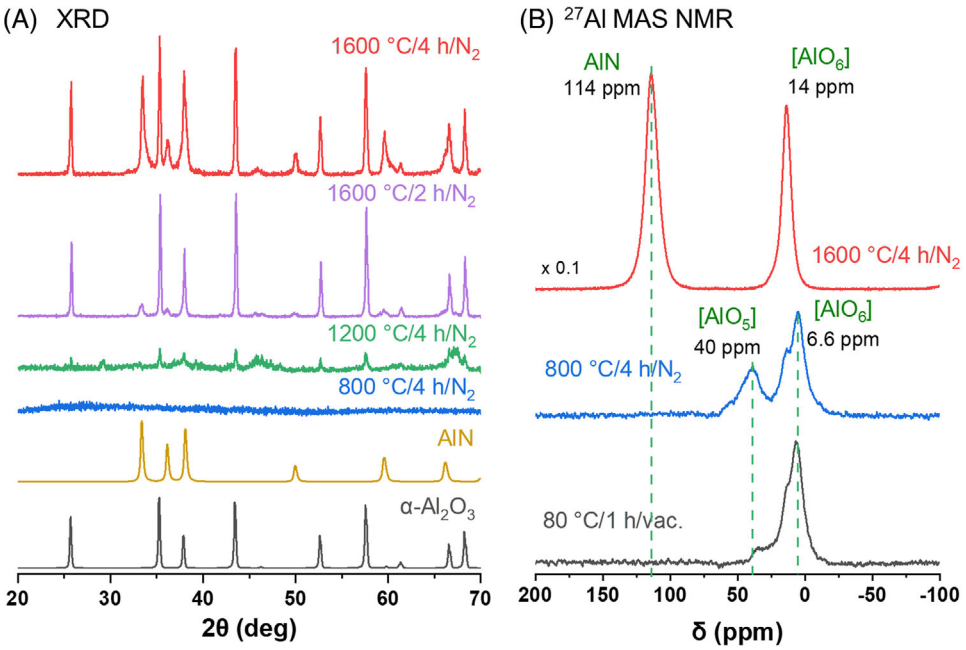

FIGURE 4 (A) X-ray powder diffractions (XRDs) of Al-HMDS pellets heated to different temperatures, compared to aluminum nitride (AlN) (hexagonal, PDF 00-025-1133) and α-Al_2O_3 (hexagonal, PDF 01-071-1683) phases. (B) ^{27}Al MAS NMR spectra of Al-HMDS powders heated to 80°C/1 h/vac, 800°, and 1600°C/4 h/N_2

80°C/1 h/vac, a peak at 6.6 ppm is observed, accompanied by a small peak at 35 ppm, revealing that Al is primarily present in [AlO_6] units with a small amount of [AlO_5] units.[53] The [AlO_5] peak intensity increased after heating to 800°C/4 h/N_2. After heating to 1600°C/4 h/N_2, a large peak at 114 ppm occurs, indicating AlN.[54–56] Another peak at 14 ppm suggests [AlO_6] units, but with different [AlO_6] peak positions and narrower when compared to Al-HMDS heated to 80° and 800°C. This suggests that the Al environment is more symmetrical for Al-HMDS heated to 1600°C, likely a result of increased crystallinity, consistent with XRD in Figure 4A.

TABLE 5 Atomic percentages (At.%) of Al-HMDS powders heated to different temperatures from energy-dispersive X-ray spectroscopy (EDX) and X-ray photoelectron spectroscopy (XPS) analyses

Analysis	Condition	O	C	N	Si	Al	Cl
EDX	80°C/1 h/vac	21.9	41.7	5.9	2.7	12.3	15.5
	800°C/4 h/N_2	30.9	23.9	9.2	1.7	29.5	4.8
	1600°C/4 h/N_2	33.7	14.3	15.4	1.1	35.5	–
XPS	1600°C/4 h/N_2	23.8	28.7	10.7	3.9	32.9	–

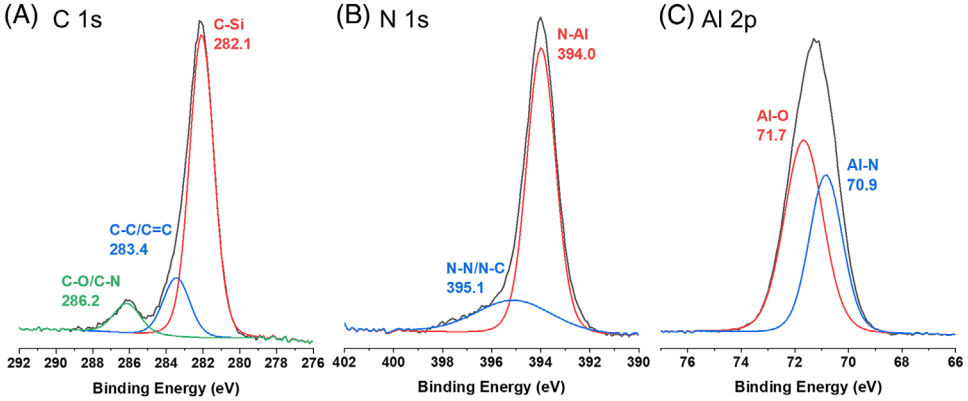

FIGURE 5 C 1s (A), N 1s (B) and Al 2p (C) core-level X-ray photoelectron (XPS) spectra of Al-HMDS pellets heated to 1600°C/4 h/N_2

Al-HMDS powders heated to different temperatures were further characterized by EDX and XPS for elemental composition analyses. Figure S5 compares SEM images and EDX maps of Al-HMDS powders heated to different temperatures. Figure S6 shows a wide-scan survey XPS spectrum of Al-HMDS heated to 1600°C/4 h/N_2. Table 5 compares atomic percentages (At.%) of Al-HMDS heated to 80–1600°C from EDX and 1600°C/4 h/N_2 from XPS analyses.

EDX analysis suggests ~15 at.% Cl content for the as-dried Al-HMDS precursor, corresponding to -Cl inclusion indicated by MALDI (Figure 1). The Cl content reduces as temperature increases and is fully eliminated after heating to 1600°C/4 h/N_2. This is in agreement with the work by Riedel et al; albeit with ammonia flow.[40] They proposed that Cl may be removed as Me_3SiCl and HCl during heat treatment and can be fully eliminated after heating to 1200°C/Ar/7 h.

EDX also shows that the C content decreases with increasing temperature, a result of organic component decomposition. Coincident obvious increases in O, N, and Al contents result at higher temperatures. Moisture uptake is likely responsible for the O content increase, as nano-sized Al-HMDS is highly susceptible to oxidation.

For Al-HMDS heated to 1600°C/4 h/N_2, both XPS and EDX analyses show similar results. Note that EDX generally has low sensitivity for O, C, and N, which can lead to inaccuracy, hence the discrepancy for O and C contents.

Core-level XPS spectra of Al-HMDS pellets heated to 1600°C/4 h/N_2 are presented in Figure 5. Three C 1s peaks are observed (Figure 5A), including a large C-Si peak at 282 eV, small peaks of C-C/C = C at 283 eV, and C-O/C-N at 286 eV. This reveals the presence of SiC when heated to 1600°C/4 h/N_2, offering potential applications for AlN/SiC refractory materials, microelectronic, and optoelectronic applications.[30,57,58]

For N 1s in Figure 5B, a large peak at 394 eV is observed, which can be ascribed to N-Al. A small broad peak appears at 395 eV, likely N-N/N-C from an amorphous phase. For Al 2p (Figure 5C), two deconvoluted peaks at 70.9 and 71.7 eV are exhibited, which can be assigned to Al-N and Al-O bonds, respectively, corresponding to AlN and Al_2O_3, as observed in XRD (Figure 4A).

3.2 | Polymer matrix with Al-HMDS powders (800°C/4 h/N_2)

As discussed above, Al-HMDS powders heated to 800°C/4 h/N_2 show the highest SSA of 250 m^2/g (Table 3), making it possible to disperse into polymer matrices to modify their thermal properties. Previously studied polymers, DGEBA-TMDS and DEO-OHS, are used as matrices. Their detailed description, synthesis methods and properties are reported elsewhere.[59] Selected amounts (5, 10, and 25 wt.%) of Al-HMDS powders heated to 800°C/4 h/N_2 were added

TABLE 6 Decomposition temperatures ($T_{d5\%}$) and ceramic yields (CYs) of composites with Al-HMDS (800°C/4 h/N_2)

Composite			
Polymer matrix	**Al-HMDS content (wt.%)**	**$T_{d5\%}$ (°C)**	**CY (%)**
DGEBA-TMDS	0	279	5
	5	284	14
	10	**291**	14
	25	275	**25**
DEO-OHS	0	238	60
	10	**340**	**62**
	25	225	52

to the matrices. Fabrication procedures for the polymer + Al-HMDS composites are provided in SI.

DGEBA-TMDS + 0–25 wt.% Al-HMDS composites are all viscous liquids. Figures S7 compares TGAs (1000°C/10°C/min/air) of pristine DGEBA-TMDS and composites with Al-HMDS, and Table 6 lists their decomposition temperatures ($T_{d5\%}$) and CYs.

Compared to pristine DGEBA-TMDS, with 5 and 10 wt.% Al-HMDS, $T_{d5\%}$ increases slightly (increments of ~5°C), and CY increases from 5 to 14 %. However, DGEBA-TMDS + 25 wt.% Al-HMDS shows a 4°C decrease for $T_{d5\%}$. Nevertheless, the overall change for $T_{d5\%}$ is very little. There is an obvious increase for the CY at 1000°C for DGEBA-TMDS + 25 wt.% Al-HMDS, which is likely due to the increased amount of Al-HMDS itself.

To make composites that form solid films, Al-HMDS (800°C/4 h/N_2) powders were added in situ to a DEO-OHS synthesis, which gels slowly and can be cast into transparent flexible thin films,[59] Figure 6A. As shown in Figure 6B,C, DEO-OHS + 10 and 25 wt.% Al-HMDS composites form black, flexible films.

Figure S8 and Table 6 reveal that with 10 wt.% Al-HMDS, $T_{d5\%}$ shows an ~100°C increment, and CY increases from 59% to 62% compared to pristine DEO-OHS, suggesting significant improvement in the polymer's thermal stability.

However, when the Al-HMDS content is further increased to 25 wt.%, both $T_{d5\%}$ and CY decrease, even lower than the pristine DEO-OHS. It is likely that the large amount of Al-HMDS, impedes the reaction between DEO and OHS as the catalyst likely binds preferentially to nitrogen, leaving considerable amounts of unreacted Si-H groups, resulting in less rigid structures with poorer thermal stabilities.

As seen in Figure S9, the IR of DEO-OHS + 25 wt.% Al-HMDS shows νSi-H with higher intensity compared to that with 10 wt.% Al-HMDS. In contrast, DEO-OHS + 10 wt.% Al-HMDS shows a much smaller νSi-H band compared to pristine DEO-OHS, indicating that a smaller amount of

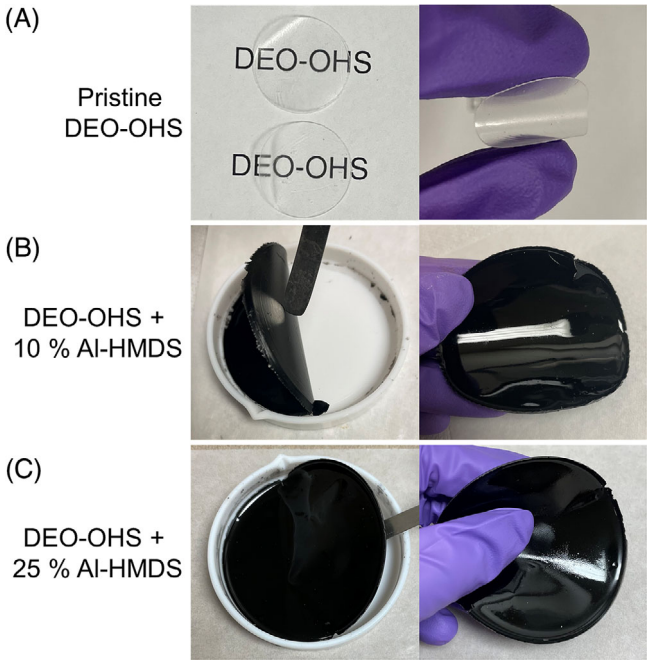

FIGURE 6 Optical images of DEO-OHS (A), DEO-OHS + 10 (B), and 25 (C) wt.% Al-HMDS (800°C/4 h/N_2) films

Al-HMDS addition may promote the reaction of DEO and OHS, resulting in improved thermal stabilities.

This also explains small improvements in $T_{d5\%}$ and CYs for DGEBA-TMDS + 5–10 wt.% Al-HMDS, and the slight decrease in $T_{d5\%}$ for DGEBA-TMDS + 25 wt.% Al-HMDS.

In conclusion, we can cast flexible solid films with Al-HMDS (800°C/4 h/N_2) powders added to DEO-OHS effectively modifying the thermal stabilities of polymer matrices with controlled loadings.

3.3 | Other M-HMDS systems

The above studies show that the reaction between $AlCl_3$ and HMDS forms Al-N bonds, and the produced Al-HMDS can be used as a precursor to AlN. In a proof-of-concept effort to extend this approach to other metal chloride systems, we briefly explored the systems Zn-HMDS, Cu-HMDS, Fe-HMDS, and Bi-HMDS. Clearly, many other metal chlorides are likely amenable to this same approach, particularly rare earth chlorides, where their nitrides offer multiple useful properties, including electrical, optical and magnetic properties, and are difficult to synthesize by traditional means because they are all high melting materials.[1,2,60]

Figure S10A–D compares FTIRs of as-synthesized Zn-HMDS, Cu-HMDS, Fe-HMDS, and Bi-HMDS precursors (dried at 80°C/1 h/vac), respectively. Similar to the Al-HMDS precursor above, they all show main peaks

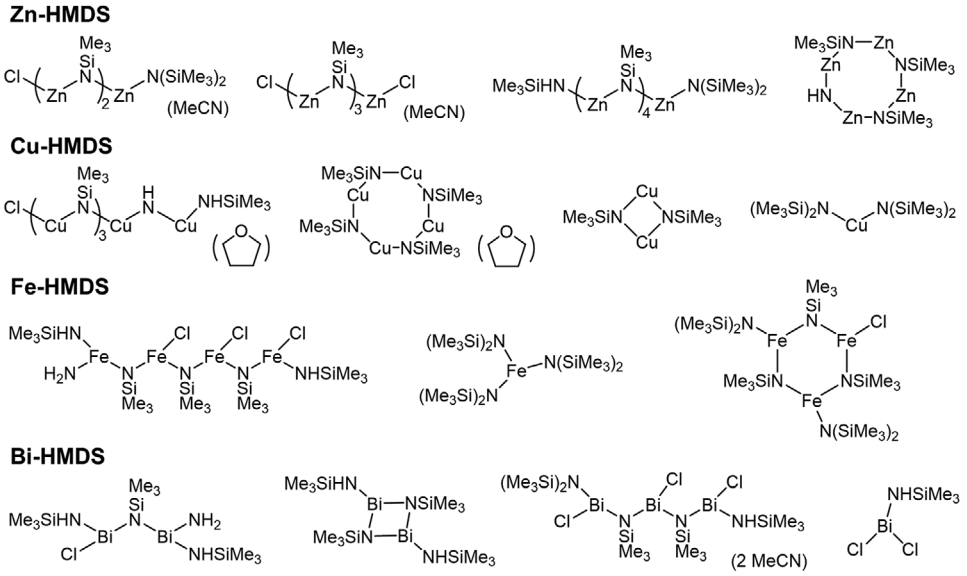

SCHEME 2 Example structures of metal-hexamethyldisilazane (M-HMDS) precursors based on matrix-assisted laser desorption/ionization (MALDI) analyses (Figure S11 and Table S2)

of νN-H at ~3100/cm, νC-H to the right of 3000/cm, an N-H overtone at ~1600/cm, δN-H/C-H at ~1400/cm, and νSi-CH_3 at ~1250/cm. Precursors reacted in ACN also exhibit νC = N at ~1700/cm, suggesting ACN may participate in the reaction or is a strongly bound solvent molecule.

These M-HMDS precursors were also characterized by both negative- and positive-ion MALDIs, Figure S11. Table S2 lists possible composition predictions based on MALDI calculations. Example structures based on MALDI analyses are shown in Scheme 2.

Overall, MALDI calculations indicate monomers, oligomers, and/or cyclomers with M-N bonds, Scheme 2. Like Al-HMDS above, -Cl inclusion and solvated complexes with THF/ACN are also predicted by some of the MALDI peaks.

^{1}H and ^{29}Si NMRs were also run on both the reaction mixtures (50 μl THF/ACN solution in 1 ml $CDCl_3$) and dried M-HMDS precursors (0.1 g/ml in $CDCl_3$). No NMR signals were observed for Cu-HMDS and Fe-HMDS precursors as the metal ions are paramagnetic.

Figure 7A compares ^{1}H NMR spectra of Zn-HMDS, HMDS, and ACN. Both the dried product and reaction mixture of Zn-HMDS show a peak at ~2 ppm, suggesting -C**H**$_3$ from ACN, likely from complexes/reactions with ACN, as also indicated by MALDI (Scheme 2). The dried product also exhibits peaks at 0.06 and 0.16 ppm, which can be ascribed to -NHSi**Me**$_3$ similar to that from HMDS, and Zn-N(H)Si**Me**$_3$, respectively. For the reaction mixture, the peaks at 0.03 ppm suggest -NHSi**Me**$_3$ (from HMDS and/or reaction products). The peak at 0.33 ppm can be ascribed to byproduct **Me**$_3$SiCl.

For ^{29}Si NMR in Figure 7B, no peaks are observed for the dried product, likely due to low solubility and/or fluxional behavior. For the reaction mixture, two peaks appear at 2.4 and 7.3 ppm. The peaks at 2.4 should be -NH**Si**Me$_3$, similar to HMDS, consistent with the ^{1}H NMR. The peak at 7.3 ppm is likely from CH_3-**Si**-Cl, Zn-N(H)**Si**Me$_3$, or a shifted CH_3-**Si**-N peak.

Figure 8A presents the ^{1}H NMR of Bi-HMDS in the reaction mixture, which shows an obvious peak at ~2 ppm from ACN, while only a very small peak at ~2 ppm is observed for the dried product, suggesting minimal interaction between the Bi-HMDS product with ACN. For the dried product, peaks at 0.06 and 0.44 ppm, and small peaks at 0.1-0.3 ppm are also found. Again, the peak at 0.06 ppm is likely -NHSi**Me**$_3$ similar to HMDS, and the peak at 0.44 ppm can be ascribed to C**H**$_3$-Si-Cl. The peaks at 0.1-0.3 ppm are likely from Bi-N(H)Si**Me**$_3$ species, given that MALDI shows mixtures of products.

For the reaction mixture, the peaks at 0.03 ppm appear to be -NHSi**Me**$_3$ from HMDS and/or reaction products, and that at 0.4 ppm can be ascribed to C**H**$_3$-Si-Cl; similar to Zn-HMDS above.

For ^{29}Si NMR in Figure 8B, again no peaks are observed for the dried product. For the reaction mixture, two ^{29}Si peaks appear at 2.3 and 7.3 ppm. Again, the interpretation is that 2.3 should be -NH**Si**Me$_3$ similar to HMDS. The peak at 7.3 ppm is likely from CH_3-**Si**-Cl, Zn-N(H)**Si**Me$_3$ or shifted CH_3-**Si**-N; again similar to the ^{29}Si NMR of Zn-HMDS above.

The Figure 9 TGA-DTAs (800-1000°C/10°C/min/N_2) were used to characterize these M-HMDS precursors with a view to their utility as ceramic precursors.

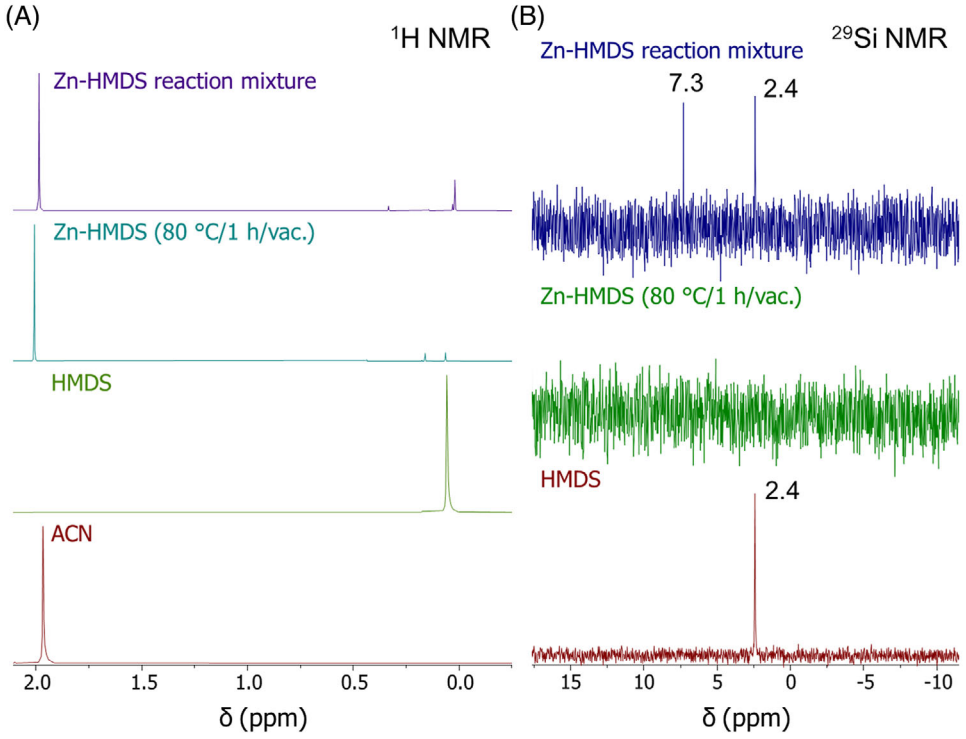

FIGURE 7 ^{1}H (A) and ^{29}Si (B) nuclear magnetic resonance (NMR) spectra of the Zn-HMDS precursor solution before and after drying (80°C/1 h/vac), compared to hexamethyldisilazane (HMDS) and tetrahydrofuran (THF)

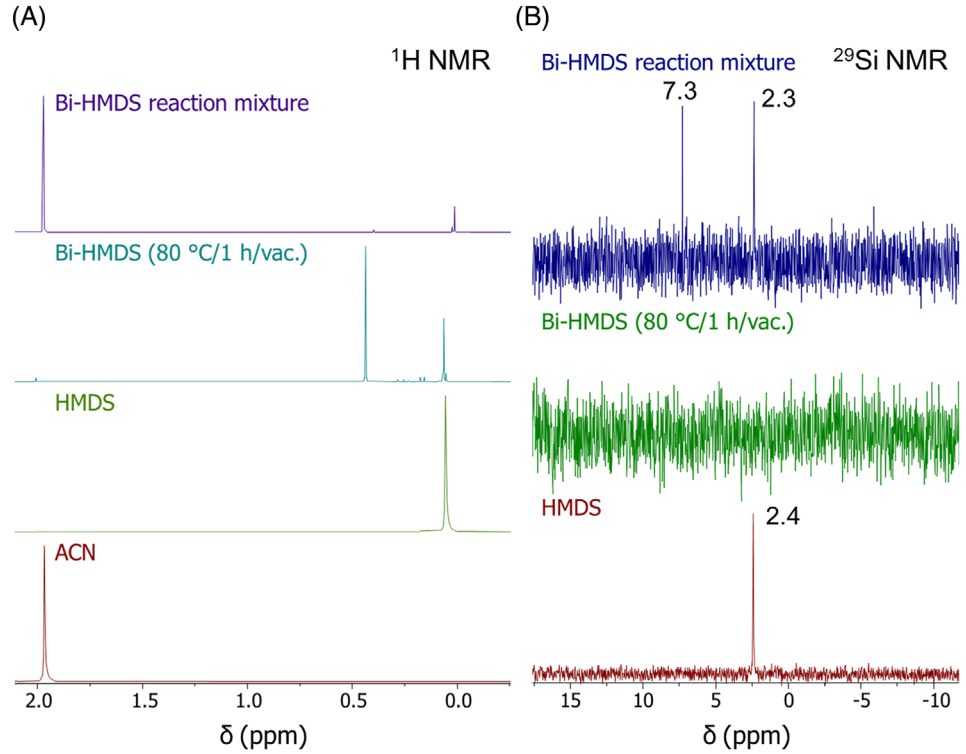

FIGURE 8 ^{1}H (A) and ^{29}Si (B) nuclear magnetic resonance (NMR) spectra of the Bi-HMDS precursor suspension before and after drying (80°C/1 h/vac), compared to hexamethyldisilazane (HMDS) and tetrahydrofuran (THF)

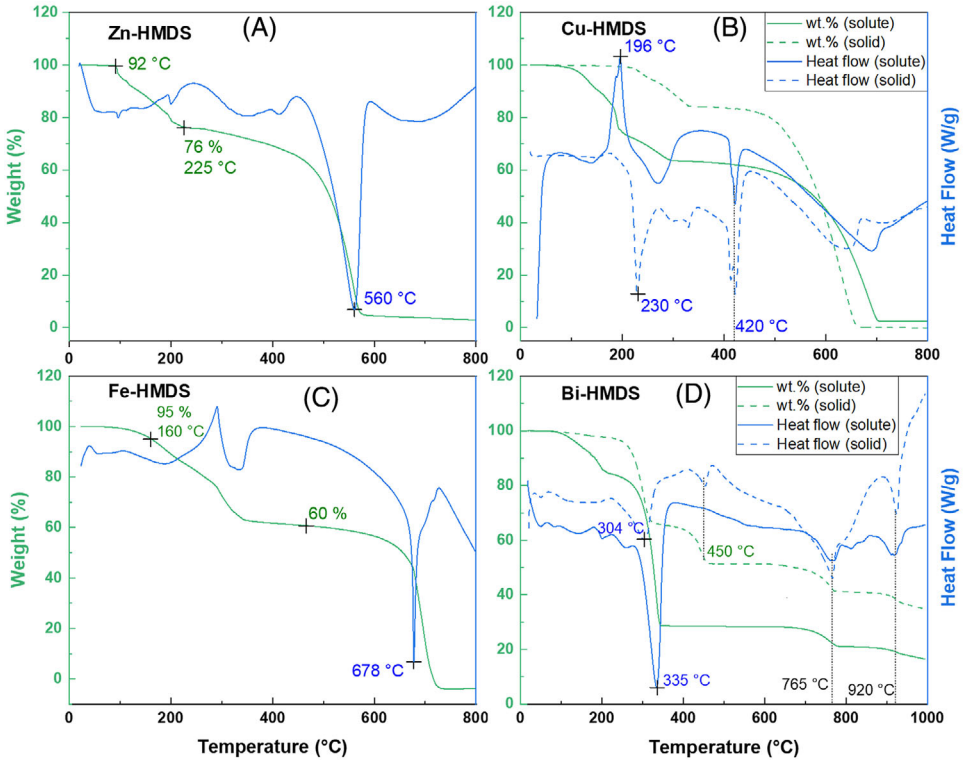

FIGURE 9 Thermogravimetric analyses-differential thermal analyses (TGA-DTAs) (800–1000°C/10°C/min/N_2) of (A) Zn-HMDS, (B) Cu-HMDS, (C) Fe-HMDS and (D) Bi-HMDS precursors dried at 80°C/1 h/vac

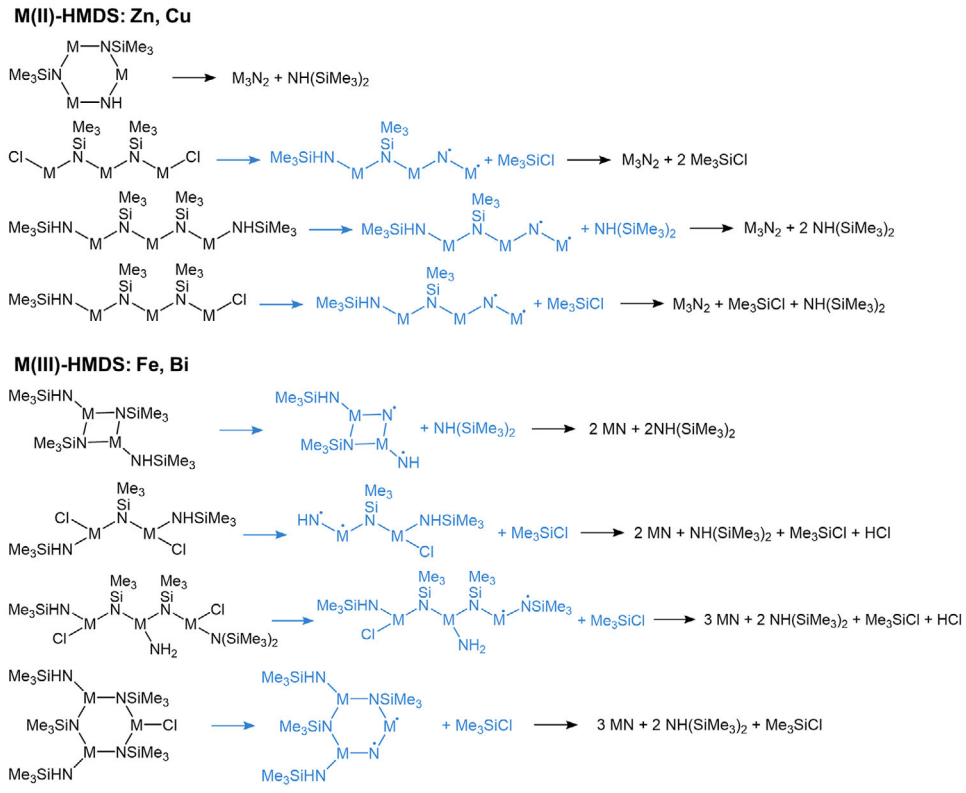

SCHEME 3 Example thermal decomposition pathways for metal-hexamethyldisilazane (M-HMDS) precursors

In general, all M-HMDS precursors show an initial mass loss at ~100–300°C, which may be volatilization of residual HMDS and Me_3SiCl, as well as decomposition of organic components. Some possible decomposition pathways are suggested in Scheme 3. When the precursors are further heated to 500–700°C, another mass loss associated with an endotherm occurs, and CY approaches 0%. This indicates sublimation/evaporation of the preceding decomposition products and/or further decomposition.

It's noteworthy that for Cu-HMDS in Figure 9B, the soluble product shows an exotherm at ~200°C, which may be crystallized, but its true nature is not yet clear. Both the soluble and insoluble parts show an endotherm without mass loss at ~420°C, which may be melting of CuCl. Indeed, the Figure S12 XRD suggests the presence of CuCl (melting point = 426°C). Although no CuCl phase is observed for the solute, there may be residual -Cl that forms CuCl as a decomposition product. Both soluble and insoluble parts show a large second mass loss at ~500–700°C, likely evaporation of melted CuCl and/or volatilization of other decomposition products as suggested in Scheme 3.

For Bi-HMDS in Figure 9D, both solute and insoluble parts show multiple mass loss procedures >400°C, suggesting stepwise decomposition/volatilization procedures.

Overall, TGA-DTA reveals the volatile nature of these M-HMDS precursors, offering the potential to be used as gas-phase deposition precursors for their corresponding metal nitrides.

4 | CONCLUSIONS

In summary, we demonstrate here a simple, novel, scalable and general route to metal nitride precursors by reactions of metal chlorides with HMDS in a solvent at low temperatures (ambient to 60°C/N_2). The primary focus of the above work targets a detailed characterization of the Al-HMDS precursor by MALDI, FTIR, TGA-DTA, NMR, XRD, XPS, and SEM/EDX. MALDI analyses suggest oligomeric/cyclomeric structures with Al-N backbone and predicted chemical environments are consistent with ^{1}H and ^{29}Si NMR studies. Al-HMDS pellets heated to 1600°C/4 h/N_2 show evidence of densification, and XRD, MAS NMR, and XPS analyses reveal the formation of AlN. However, Al_2O_3 is also presented, resulting from high susceptibility to oxidation due to the high SSAs (>200 m^2/g). Al-HMDS powders heated to 800°C/4 h/N_2 show the highest SSA of 252 m^2/g, and they are able to disperse into polymer matrices to modify their thermal stabilities with controlled loadings.

Other metal chloride systems were also briefly explored including Zn-HMDS, Cu-HMDS, Fe-HMDS, and Bi-HMDS, as potential precursors to corresponding metal nitrides. MALDI study indicates oligomers/cyclomers with M-N bonds, similar to Al-HMDS. TGA-DTA suggests that these M-HMDS precursors are volatile when heated (typically 500–700°C), providing the potential to be used as gas-phase deposition precursors for their corresponding metal nitrides.

ACKNOWLEDGMENTS

We are grateful for the support of a significant portion of this work by NSF DMR Grant No. 1926199 and a gift from Mercedes Benz Research and Development North America (MBRDNA), Redford, MI, USA. We also would like to thank Andrew Alexander for his assistance in developing the computer program for precursor composition calculations based on MALDI-ToF.

ORCID

Xinyu Zhang https://orcid.org/0000-0003-2971-9185
Sylvio Indris https://orcid.org/0000-0002-5100-113X
Richard M. Laine https://orcid.org/0000-0003-4939-3514

REFERENCES

1. Giordano C, Antonietti M. Synthesis of crystalline metal nitride and metal carbide nanostructures by sol–gel chemistry. Nano Today. 2011;6(4):366–80.
2. Ashraf I, Rizwan S, Iqbal M. A comprehensive review on the synthesis and energy applications of nano-structured metal nitrides. Front Mater. 2020;7:181.
3. Kindlund H, Sangiovanni DG, Petrov I, Greene JE, Hultman L. A review of the intrinsic ductility and toughness of hard transition-metal nitride alloy thin films. Thin Solid Films. 2019;688:137479.
4. Didziulis SV, Butcher KD, Perry SS. Small cluster models of the surface electronic structure and bonding properties of titanium carbide, vanadium carbide, and titanium nitride. Inorg Chem. 2003;42(24):7766–81.
5. Shafiee SA, Perry SC, Hamzah HH, Mahat MM, Al-lolage FA, Ramli MZ. Recent advances on metal nitride materials as emerging electrochemical sensors: a mini review. Electrochem Commun. 2020;120:106828.
6. Navinsek B, Seal S. Transition metal nitride functional coatings. J Miner Met Mater Soc. 2001;53(9):51–4.
7. Wolf W, Podloucky R, Antretter T, Fischer FD. First-principles study of elastic and thermal properties of refractory carbides and nitrides. Philos Mag B. 1999;79(6):839–58.
8. Wittmer M. TiN and TaN as diffusion barriers in metallizations to silicon semiconductor devices. Appl Phys Lett. 1980;36(6):456–8.
9. Kim H. Atomic layer deposition of metal and nitride thin films: current research efforts and applications for semiconductor device processing. J Vac Sci Tech B. 2003;21(6):2231–61.

10. O'Leary SK, Foutz BE, Shur MS, Eastman LF. Steady-state and transient electron transport within the III–V nitride semiconductors, GaN, AlN, and InN: a review. J Mater Sci: Mater El. 2006;17(2):87–126.
11. Mühlbacher M, Greczynski G, Sartory B, Schalk N, Lu J, Petrov I, et al. Enhanced $Ti_{0.84}Ta_{0.16}N$ diffusion barriers, grown by a hybrid sputtering technique with no substrate heating, between Si(001) wafers and Cu overlayers. Sci Rep. 2018;8(1):5360.
12. Xie J, Xie Y. Transition metal nitrides for electrocatalytic energy conversion: opportunities and challenges. Chem Eur J. 2016;22(11):3588–98.
13. Dong S, Chen X, Zhang X, Cui G. Nanostructured transition metal nitrides for energy storage and fuel cells. Coord Chem Rev. 2013;257(13):1946–56.
14. Zhong Y, Xia X, Shi F, Zhan J, Tu J, Fan HJ. Transition metal carbides and nitrides in energy storage and conversion. Adv Sci. 2016;3(5):1500286.
15. Iqbal A, Mohd-Yasin F. Reactive sputtering of aluminum nitride (002) thin films for piezoelectric applications: a review. Sensors 2018;18(6):1797.
16. Nam K, Hong K, Park H, Choe H. Facile synthesis of powder-based processing of porous aluminum nitride. J Eur Ceram Soc. 2018;38(4):1164–9.
17. Qadri SB, Gorzkowski EP, Rath BB, Feng CR, Amarasinghe R. Synthesis and characterization of nanoparticles of wurtzite aluminum nitride from various nut shells. J Alloys Compd. 2017;708:67–72.
18. Gundel P, Bawohl M, Challingsworth M, Choisi M, Garcia V & Gaul M et al. Thick printed copper as highly reliable substrate technology for power electronics. In: proceedings of PCIM Europe 2015; International exhibition and conference for power electronics, intelligent motion, renewable energy and energy management. Nuremberg, Germany: VDE Verlag; 19-20 May 2015. p. 1–6. https://ieeexplore.ieee.org/abstract/document/7149164/authors#authors
19. Seppänen H, Kim I, Etula J, Ubyivovk E, Bouravleuv A, Lipsanen H. Aluminum nitride transition layer for power electronics applications grown by plasma-enhanced atomic layer deposition. Materials 2019;12(3):406.
20. Wu P, Funato M, Kawakami Y. Environmentally friendly method to grow wide-bandgap semiconductor aluminum nitride crystals: elementary source vapor phase epitaxy. Sci Rep. 2015;5(1):17405.
21. Hou Y, Zhang M, Han G, Si C, Zhao Y, Ning J. A review: aluminum nitride MEMS contour-mode resonator. J Semicond. 2016;37(10):101001.
22. Jakkaraju R, Henn G, Shearer C, Harris M, Rimmer N, Rich P. Integrated approach to electrode and AlN depositions for bulk acoustic wave (BAW) devices. Microelectron Eng. 2003;70(2):566–70.
23. Zhao S, Connie AT, Dastjerdi MHT, Kong XH, Wang Q, Djavid M, et al. Aluminum nitride nanowire light emitting diodes: breaking the fundamental bottleneck of deep ultraviolet light sources. Sci Rep. 2015;5(1):8332.
24. Liu G, Zhou G, Qin Z, Zhou Q, Zheng R, Wu H, et al. Luminescence characterizations of freestanding bulk single crystalline aluminum nitride towards optoelectronic application. Cryst Eng Comm. 2017;19(37):5522–7.
25. Baik Y, Drew RAL. Aluminum nitride: processing and applications. Key Eng Mater. 1996;122–124:553.
26. Elagin AA, Beketov AR, Baranov MV, Shishkin RA. Aluminum nitride. Preparation methods (review). Refract Ind Ceram. 2013;53(6):395–403.
27. Hwang B-H, Chen C-S, Lu H-Y, Hsu T-C. Growth mechanism of reactively sputtered aluminum nitride thin films. Mater Sci Eng A. 2002;325(1):380–8.
28. Timoshkin AY, Bettinger HF, Schaefer HF. The chemical vapor deposition of aluminum nitride: unusual cluster formation in the gas phase. J Am Chem Soc. 1997;119(24):5668–78.
29. Khan AH, Odeh MF, Meese JM, Charlson EM, Charlson EJ, Stacy T, et al. Growth of oriented aluminium nitride films on silicon by chemical vapour deposition. J Mater Sci. 1994;29(16):4314–8.
30. Tanaka S, Kern RS, Davis RF. Initial stage of aluminum nitride film growth on 6H-silicon carbide by plasma-assisted, gas-source molecular beam epitaxy. Appl Phys Lett. 1995;66(1):37–9.
31. Karmann S, Schenk HPD, Kaiser U, Fissel A, Richter W. Growth of columnar aluminum nitride layers on Si(111) by molecular beam epitaxy. Mater Sci Eng B. 1997;50(1):228–32.
32. Rosenberger L, Baird R, McCullen E, Auner G, Shreve G. XPS analysis of aluminum nitride films deposited by plasma source molecular beam epitaxy. Surf Interface Anal. 2008;40(9):1254–61.
33. Vispute RD, Wu H, Narayan J. High quality epitaxial aluminum nitride layers on sapphire by pulsed laser deposition. Appl Phys Lett. 1995;67(11):1549–51.
34. Lu YF, Ren ZM, Chong TC, Cheong BA, Chow SK, Wang JP. Ion-assisted pulsed laser deposition of aluminum nitride thin films. J Appl Phys. 2000;87(3):1540–2.
35. Erwin SC, Lyons JL. Atomic layer epitaxy of aluminum nitride: unraveling the connection between hydrogen plasma and carbon contamination. ACS Appl Mater Interfaces. 2018;10(23):20142–9.
36. Anderson VR, Nepal N, Johnson SD, Robinson ZR, Nath A, Kozen AC, et al. Plasma-assisted atomic layer epitaxial growth of aluminum nitride studied with real time grazing angle small angle x-ray scattering. J Vac Sci Technol A. 2017;35(3):031508.
37. Zhang X, Temeche E, Laine RM. Design, synthesis, and characterization of polymer precursors to Li_xPON and Li_xSiPON glasses: materials that enable all-solid-state batteries (ASBs). Macromolecules 2020;53(7):2702–12.
38. Temeche E, Zhang X, Laine RM. Polymer precursor derived Li_xPON electrolytes: toward Li–S batteries. ACS Appl Mater Interfaces. 2020;12(18):20548–62.
39. Giordano C, Corbiere T. A step forward in metal nitride and carbide synthesis: from pure nanopowders to nanocomposites. Colloid Polym Sci. 2013;291(6):1297–311.
40. Riedel R, Petzow G, Klingebiel U. Characterization of AlN powder produced by the reaction of $AlCl_3$ with hexamethyldisilazane. J Mater Sci Lett. 1990;9:222–4.
41. Amonoo-Neizer EH, Shaw RA, Skovlin DO, Smith BC, Rosenthal JW, Jolly WL. Lithium bis(trimethylsilyl)amide and tris(trimethylsilyl)amine. Inorganic Syntheses, Volume 8. 1966:19–22. https://onlinelibrary.wiley.com/doi/abs/10.1002/9780470132395.ch6

42. Wannagat U, Niederprüm H. Beiträge zur chemie der silicium-stickstoff-verbindungen, XIII. Silylsubstituierte alkaliamide. Chem Ber. 1961;94(6):1540–7.
43. Schüler P, Görls H, Westerhausen M, Krieck S. Bis(trimethylsilyl)amide complexes of s-block metals with bidentate ether and amine ligands. Dalton Trans. 2019;48(24):8966–75.
44. Eller PG, Bradley DC, Hursthouse MB, Meek DW. Three coordination in metal complexes. Coord Chem Rev. 1977;24(1):1–95.
45. Alyea EC, Bradley DC, Copperthwaite RG. Three-coordinated transition metal compounds. Part I. The preparation and characterization of tris(bistrimethylsilylamido)-derivatives of scandium, titanium, vanadium, chromium, and iron. J Chem Soc Dalton Trans. 1972;(14):1580–4.
46. Edelmann FT, Pauer F, Wedler M, Stalke D. Preparation and structural characterization of dioxane-coordinated alkali metal bis(trimethylsilyl)amides. Inorg Chem. 1992;31(20):4143–6.
47. Krieck S, Schüler P, Görls H, Westerhausen M. Straightforward synthesis of rubidium bis(trimethylsilyl)amide and complexes of the alkali metal bis(trimethylsilyl)amides with weakly coordinating 2,2,5,5-tetramethyltetrahydrofuran. Dalton Trans. 2018;47(36):12562–9.
48. Zhang X, Temeche E, Laine RM. Li_xSiON ($x = 2, 4, 6$): a novel solid electrolyte system derived from agricultural waste. Green Chem. 2020;22(21):7491–505.
49. Arshadi M, Johnels D, Edlund U, Ottosson CH, Cremer D. Solvated silylium cations: structure determination by NMR spectroscopy and the NMR/Ab initio/IGLO method. J Am Chem Soc. 1996;118(21):5120–31.
50. Mourya S, Jaiswal J, Malik G, Kumar B, Chandra R. Structural and optical characteristics of in-situ sputtered highly oriented 15R-SiC thin films on different substrates. J Appl Phys. 2018;123(2):023109.
51. Taborda JAP, Caicedo JC, Grisales M, Saldarriaga W, Riascos H. Deposition pressure effect on chemical, morphological and optical properties of binary Al-nitrides. Opt Laser Technol. 2015;69:92–103.
52. Djebaili K, Mekhalif Z, Boumaza A, Djelloul A. XPS, FTIR, EDX, and XRD analysis of Al_2O_3 scales grown on PM2000 alloy. J Spectrosc. 2015;2015:868109.
53. Bräuniger T, Jansen M. Solid-state NMR Spectroscopy of quadrupolar nuclei in inorganic chemistry. Z Anorg Allg Chem. 2013;639(6):857–79.
54. Dupree R, Lewis MH, Smith ME. Structural characterization of ceramic phases with high-resolution ^{27}Al NMR. J Appl Crystallogr. 1988;21:109–16.
55. Bräuniger T, Kempgens P, Harris RK, Howes AP, Liddell K, Thompson DP. A combined $^{14}N/^{27}Al$ nuclear magnetic resonance and powder X-ray diffraction study of impurity phases in β-sialon ceramics. Solid State Nucl Magn Reson. 2003;23(1):62–76.
56. Zeman OEO, Moudrakovski IL, Hartmann C, Indris S, Bräuniger T. Local electronic structure in AlN studied by single-crystal ^{27}Al and ^{14}N NMR and DFT calculations. Molecules 2020;25(3):469.
57. Helava HI, Mokhov EN, Avdeev OA, Ramm MG, Litvin DP, Vasiliev AV, et al. Growth of low-defect SiC and AlN crystals in refractory metal crucibles. Mater Sci Forum. 2013;740–742:85–90.
58. Meinschien J, Falk F, Hobert H, Stafast H. Deposition of SiC and AlN thin films by laser ablation. Appl Surf Sci. 1999;138–139:543–8.
59. Zhang X, Yu M, Laine RM. An approach to epoxy resins: oxysilylation of epoxides. Macromolecules 2020;53(6):2249–63.
60. Didchenko R, Gortsema FP. Some electric and magnetic properties of rare earth monosulfides and nitrides. J Phys Chem Solids. 1963;24(7):863–70.

SUPPORTING INFORMATION

Additional supporting information may be found in the online version of the article at the publisher's website.

How to cite this article: Zhang X, Yu M, Indris S, Laine RM. Reactions of metal chlorides with hexamethyldisilazane: Novel precursors to aluminum nitride and beyond. J Am Ceram Soc. 2022;105:2474–2488.
https://doi.org/10.1111/jace.18271